Broadband Black-Phosphorus Photodetectors with High Responsivity

*Mingqiang Huang, Mingliang Wang, Cheng Chen, Zongwei Ma, Xuefei Li, Junbo Han, and Yanqing Wu**

Extensive research on photodetectors based on novel 2D materials such as graphene and transition metal dichalcogenides (TMDs) have been carried out recently because of their wide application in photodetection, imaging, and telecommunications.[1] It is of great interest to find novel functional materials not only with high photoresponsivity (R), but also in a broadband spectral range.[2–4] Owing to the gapless nature, graphene has a strong interaction with photons in a very wide spectral range.[5–15] However, the photoresponsivity of graphene photodetectors are usually quite small because of the small light absorption of 2.3% per layer, resulting in a limited photocarrier generation. Many efforts have been spent on resolving this bottleneck such as bandgap engineering and heterogeneous integration with quantum dots.[16] Nevertheless, these methods either require extensive nanopatterning or complicated fabrication process, which will affect not only their repeatability, but also the throughput as well as large-scale integration. The emerging TMDs such as single layer MoS_2 exhibit excellent photodetection properties due to their direct bandgap.[17,18] However, these photodetectors usually have limited use only in a narrow visible spectral range because of the large bandgaps.[19–22]

Black phosphorus (BP) is an elemental 2D semiconducting material,[23–26] with a direct bandgap of around 1.5 eV for monolayer and down to 0.3 eV in bulk.[27] Such a narrow bandgap covering the spectral range from visible to near-infrared makes BP a very promising candidate for broadband optoelectronic applications. In addition to the high carrier mobility, few-layer BP has a direct bandgap and strong light absorption efficiency in broadband spectrum, all of which are crucial factors for high-performance photodetection.[28–42] However, previous results show that the largest R observed in BP photodetectors is only several hundreds of mA W^{-1},[33–36] which is far below the TMDs counterpart.[21,22] Recently, colossal ultraviolet R of 10^5 A W^{-1} has been demonstrated using BP photodetector.[37] Despite of its high performance in the UV region, the photoresponsivity dropped dramatically for almost five orders of magnitude as the excitation wavelength increases beyond 500 nm. Furthermore, no photodetection on black-phosphorus photodetector at low temperature has been carried out. In order to address these issues, here we demonstrate high-performance BP photodetectors with photoresponsivity in a broad range from 400 to 900 nm, as well as quantitative analysis photoresponse at different temperatures from 300 down to 20 K.

The BP photodetectors reported here are based on back-gate field-effect transistor (FET) configuration as shown in the schematic view of **Figure 1**a. Few-layer BP flakes are obtained using mechanical exfoliation onto a 90 nm SiO_2 substrate. Then, source/drain electrodes were patterned by electron-beam (e-beam) lithography and Ni/Au metal contact was deposited by e-beam evaporation. The fabricated short channel transistors are shown in Figure 1b using atomic force microscopy (AFM). The thickness of BP flake is measured to be 8 nm, corresponding to 15 layers as depicted in Figure 1d. Raman spectrum is shown in Figure 1c, where three Raman peaks at 362.2, 439.8, and 467.6 cm^{-1} agree well with previous observations for multilayer BP.[35,38,43] In our experiment, the sample was put in a cryogenic lakeshore probe station and all measurements were carried out in high vacuum of 2×10^{-4} mbar. The optical measurement was performed using a femtosecond laser guided through an optical fiber and the probe arm was very close to the sample. The laser wavelength was kept at 633 nm for most measurements, and then changed to 400 and 900 nm for the remaining measurements.

Output characteristics of the 1 μm BP FET in dark and under illumination measured at 300 and 20 K are shown in **Figure 2**a,b, respectively. The incident laser power density is fixed at 250 mW cm^{-2} with a wavelength of 633 nm. It is clear that the photocurrent generated increases when gate bias and drain bias increase. Moreover, the photocurrent also increases when the temperature is reduced to 20 K. The mechanism of the photodetector is dominated by photoconductive effect in our devices, because of the linear relationship of the output current and drain voltage. This transverse-field dependence becomes less linear when the temperature decreases to 20 K, when the Schottky barrier at source/drain junction starts to dominate the carrier transport.[44,45] More details can be seen in Figure S1 (Supporting Information). To better characterize the photocurrent dependence on gate bias and drain bias at different temperatures, we carried out systematic photocurrent measurements as depicted in Figure 2c,d. It can be seen that the photoresponse increases greatly at low temperature, where the photocurrent (I_{ph}) is about 32 μA ($I_{ph}/I_{dark} \approx 18\%$) at 20 K and 4 μA ($I_{ph}/I_{dark} \approx 3.5\%$) at 300 K. As stated above, the linear dependence of photocurrent on the drain voltage can be better visualized in these contour plots and further confirms photoconduction model.[2–4] Photons with energy greater than

M. Huang, M. Wang, C. Chen, Z. Ma, Dr. X. Li, Prof. J. Han, Prof. Y. Wu
Wuhan National High Magnetic Field Center and School of Physics
Huazhong University of Science and Technology
Wuhan 430074, P. R. China
E-mail: yqwu@mail.hust.edu.cn
M. Wang, Dr. X. Li, Prof. Y. Wu
School of Optical and Electronic Information
Huazhong University of Science and Technology
Wuhan 430074, P. R. China

DOI: 10.1002/adma.201506352

ADVANCED MATERIALS
www.advmat.de

Materials Views
www.MaterialsViews.com

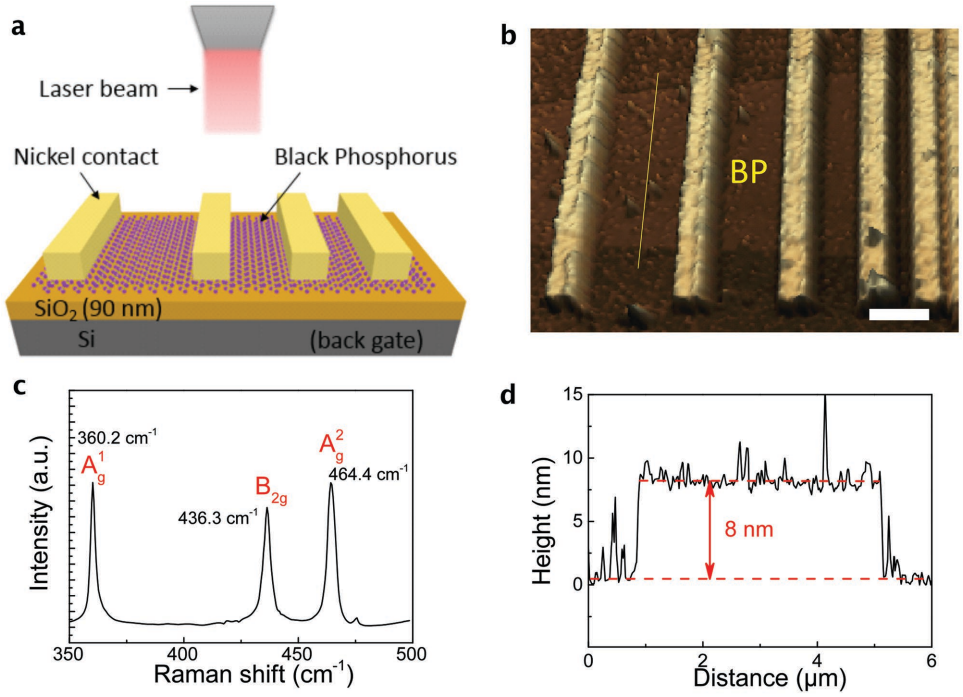

Figure 1. Schematic view of the device. a) Cross-section view of the device fabricated in this work. The contact electrode metal is Ni/Au. The gate dielectric is 90 nm SiO_2. b) 3D topography of the device scanned in AFM. The scale bar is 1 μm. c) Raman measurement of the BP film. d) The measured data of the yellow line in (b) and the thickness is 8 nm corresponding to 15 layers of BP.

the bandgap can be easily absorbed and generate electron–hole pairs in this direct bandgap semiconductor. Under a transverse electric field, these excess carriers will be separated and drift to the collecting ends.[2,3] Moreover, we notice that photocurrent can only be clearly observed at the on-state and minimal photoresponse exists at the off-state (Figure S2, Supporting Information), which is different from some of the TMD-based photodetectors.[20,21] The main reason is in this back-gated

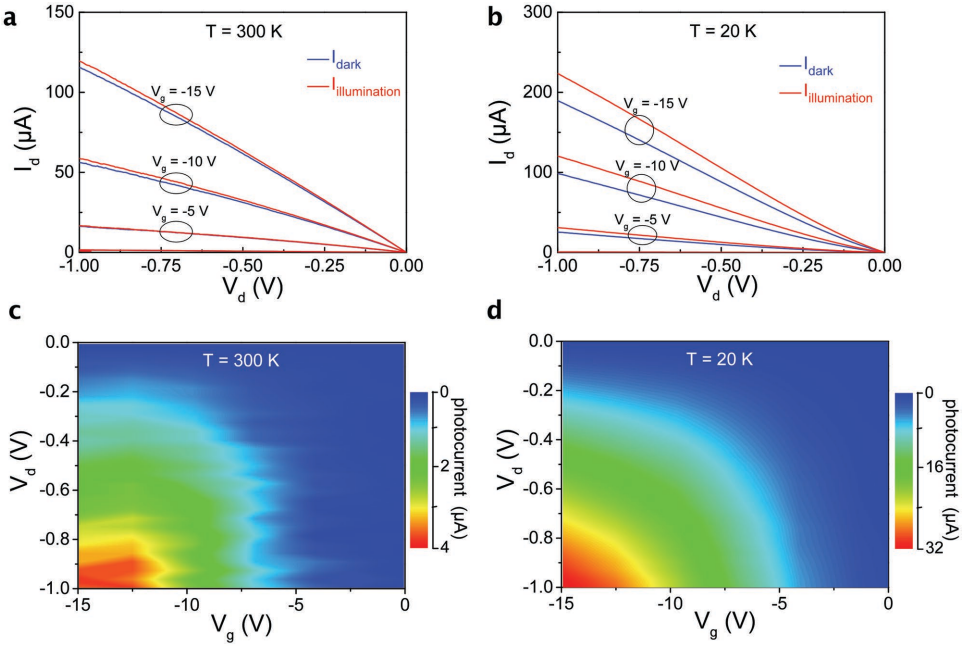

Figure 2. Electronic and optoelectronic characteristics of the 1 μm device. a) The output characteristic curves of the device at 300 K. The blue and red line represents the drain current in dark or under illumination (λ = 633 nm, P = 250 mW cm^{-2}), respectively. The backgate voltage V_g changes from −15 to 0 V, and the step is 5 V. b) Electronic and optoelectronic characteristics of the device at 20 K. All the detection conditions are the same as in panel (a). c,d) Color contour plot of the photocurrent extracted from panel (a) and (b).

Adv. Mater. 2016,
DOI: 10.1002/adma.201506352

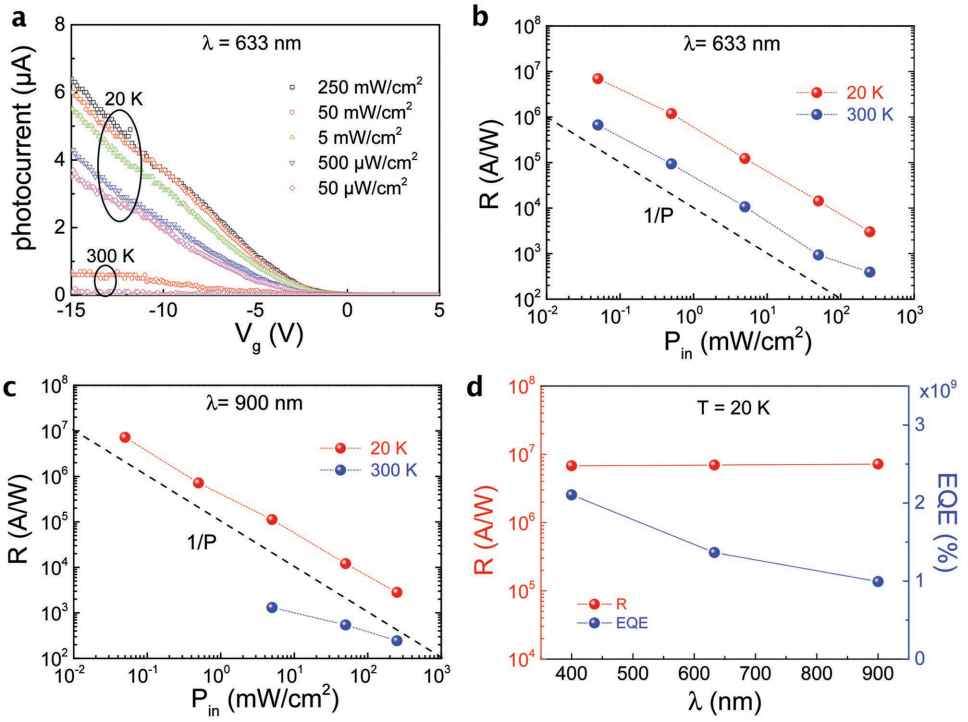

Figure 3. Photoresponse of the 1 μm device. a) Photo-generated current in backgate-voltage-dependent photodetection under different laser power density. A fair comparison between 20 and 300 K has been shown. The incident laser wavelength is 633 nm and the drain voltage is $V_d = -0.2$ V. b,c) R of the device at different incident laser power. All data are extracted at the bias voltage of $V_g = -15$ V, $V_d = -1$ V. The wavelength of the incident laser is 633 and 900 nm in panels (b) and (c), respectively. At 300 K, the device shows weak response to 900 nm laser, and the cut-off point is 5 mW cm^{-2}. While at 20 K, they exhibit little difference. d) External quantum efficiency for different kinds of incident photons.

structure, the gate voltage not only modulates the carrier density in the channel, but also changes the Schottky barrier height and shape near the source/drain contact.[31] At the off-state, the Schottky barrier height is the highest and the probability of the photogenerated carriers reaching the collecting ends becomes negligible.

As shown in **Figure 3**a, the photoresponse of the same 1 μm device with different incident laser power density are studied as it decreases from 250 mW cm^{-2} down to 50 μW cm^{-2} at 633 nm wavelength measured at 300 and 20 K. It is clear that the photocurrent increases with increasing laser power and moreover, distinct photocurrent can be observed even at the lowest power density of 50 μW cm^{-2} at 20 K. This high sensitivity to weak photosignal has surpassed all previous BP photodetectors,[33–37,40,46,47] where the power density is usually in the range of 2 mW cm^{-2} or much higher. The photocurrent increases several times when the measurement temperature is decreased from 300 to 20 K, which can be attributed to the improved carrier generation-recombination rate and better carrier transport at low temperatures which will be discussed in detail later.

Photoresponsivity and the quantum efficiency as well as the photoresponse spectral range are among the most important figures-of-merit in photodetectors.[2,48,49] Here, two representative wavelengths at 633 and 900 nm are used and the corresponding R of this device are plotted in Figure 3b,c, respectively. At room temperature, it shows very strong photoresponse to the incident photons from visible to near-infrared spectrum. A high photoresponsivity $R = 6.7 \times 10^5$ A W^{-1} for 633 nm can be achieved, which is six orders larger than the previously reported BP-based photodetectors at the same wavelength.[34,46,47] In the near-infrared region of 900 nm, a high responsivity about 10^3 A W^{-1} at 300 K and 7×10^6 A W^{-1} at 20 K has been achieved for the first time. By fitting the experimental data using a simple power law dependence $R \approx P^{\alpha}$, we can deduce the factor α to be about −0.90 that is close to the ideal saturation factor $\alpha = -1$ for all data except the 900 nm at 300 K, which may be disturbed by the environment. As summarized in Figure 3d, the external quantum efficiency shows an increasing trend from 900 to 400 nm, which can be attributed to the increased photon energy. Compared to previous work with the same device configuration, our devices show much smaller contact resistance, which greatly improves the on current and thus the photocurrent. By using a contact metal like Ni which forms a good ohmic contact to BP under p-type operation in our devices, the photogenerated carriers can be collected at the source/drain end with a much higher efficiency. We note here that metals with large work function such as Pd may also lead to good ohmic contact for p-type operations and better device performance can be achieved with further optimizations for ohmic formation.

For a narrow bandgap material like BP, another important feature of the transistor is ambipolar behavior.[31] BP FETs can be operated in both n-type and p-type regimes by changing the backgate voltage. In order to better understand the photoconductive mechanism and the role of the Schottky barrier in these ambipolar devices, we measured both p-type and n-type

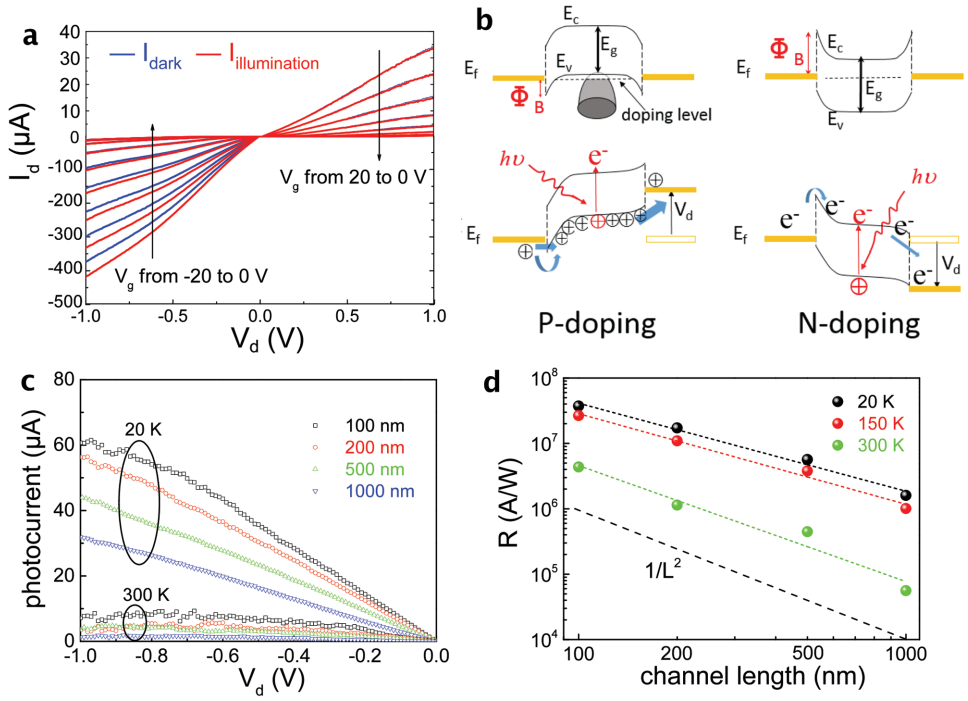

Figure 4. Length-scaling dependence on the photoresponse. a) Asymmetric photoresponse of the device featuring a very short channel length $L = 100$ nm at the condition of $T = 150$ K, $\lambda = 633$ nm, $P = 0.5$ mW cm^{-2}. b) Typical energy-band diagram of the semiconductor black phosphorus. The left and right panel illustrates the hole and electron injection regions, respectively. The up and down panel shows the device under zero- and operating-bias voltage, respectively. c) Channel-length dependence of the photogenerated current at 20 and 300 K. The channel width of the four devices is about the same (4.5 μm). The incident laser power density is fixed at 0.5 mW cm^{-2}. d) Photoresponsivity of the devices under the same driving voltage ($V_g = -20$ V, $V_d = -1$ V). An improved optoelectronic characteristic with inverse channel length squared dependence has been observed.

photodetection of a short channel 100 nm device as shown in **Figure 4**a. Interestingly, the photoresponse shows very asymmetric behavior where the photocurrent only exists in the p-type FET. To further explore the mechanisms of the asymmetry, band diagrams of the device under both types of operations are illustrated in Figure 4b. The photoinduced carriers can be easily generated at both p-branch and n-branch without distinction, however, during the transport and collection, the Schottky barrier height is much higher in the n-type region and makes it much more difficult for electrons to travel from the source end. As a result, the photocurrent is strongly suppressed in the n-branch, which also explains the minimal photocurrent in the off-state. As plotted in Figure 4c, the photocurrent of various devices with different channel lengths are measured at 300 and 20 K, and as the channel length decreases, the photocurrent increases mainly due to the larger transverse electric field and smaller transit time. The calculated photoresponsivity for various channel lengths has been plotted in Figure 4d. The 100 nm device shows a record-high R of 4.3×10^6 A W^{-1} at 300 K, which is two orders of magnitude higher than that of the 1 μm device. This improved photoresponsivity has a clear inversely proportional dependence on channel length squared. Because $R \propto EQE = \frac{\tau_{\text{lifetime}}}{\tau_{\text{transit}}}$, where τ_{lifetime} is the lifetime of the photo-induced carrier, τ_{transit} is the carrier transfer time, and this leads to the linear dependence of photoresponsivity to the inverse of carrier transit time. Meanwhile, the transit time can be calculated by $\tau_{\text{transit}} = \frac{L^2}{\mu V_{\text{ds}}}$, where L is the channel length, μ is the carrier mobility, and V_{ds} is the drain-source voltage. Therefore, a simplified relationship of responsivity against channel length can be deduced which is consistent with the above results. This result confirms the photoconductive mechanism and indicates that further performance enhancement can be achieved by continuous scaling of the channel lengths to sub-100 nm. The temperature dependent photoresponse can also be observed in Figure 4c,d, which shows improvements in not only photodetection, but also in sensitivity to low laser power. We attribute this improvement to the freezing of interface and bulk traps which easily captures the electron–hole pairs and introduces extra scattering, and also the reduced phonon scattering which affects the mobility.[45] We also note that this device exhibits a very fast response time with $\tau_{\text{rise}} = 5$ ms (the resolution limit of the testing system) as shown in Figure S5 (Supporting Information).

In summary, we have demonstrated a high-performance broadband BP-based photodetector in the wavelength range from 400 to 900 nm. The record-high photoresponsivity reaches up to about 7×10^6 A W^{-1} at 20 K and 4.3×10^6 A W^{-1} at 300 K for the 100 nm device in a broadband spectrum. A systematic study of the photoresponse dependence on temperature, incident laser power density, photon energy, and channel length for BP-based photodetectors is carried out for the first time. These performance parameters are among the best in the 2D materials-based photodetectors reported so far, showing great potential of black phosphorus in the application of broadband photodetection at a wide temperature range.

Adv. Mater. **2016**,
DOI: 10.1002/adma.201506352

Experimental Section

Fabrication: Few-layer black phosphorus was mechanically exfoliated and identified under a microscope in a glove box, where the oxygen and water contents are always kept below 0.1 ppm. Standard electron-beam lithography and electron-beam evaporation are used to form the device structures and metal contacts. During the whole fabrication, the sample was always kept in the glove box; in-between process steps the time of exposure to air was minimized.

AFM: Atomic force microscopy (Shimadzu SPM-9700) was used to determine the thickness of BP flakes. It was operated in tapping mode to measure the topography and to determine the number of BP layers.

Optoelectronic Characterization: The device was placed inside an electrically shielded and optically sealed probe station system (Lakeshore CPX-VF). A 3D adjustable optical fiber was used to guide the laser from a tunable Ti:Sapphire laser system onto the device. In the measurement, the sample was placed inside an electrical shielded and optical sealed probe station system. Mounts of photons were generated in a tunable Ti:Sapphire laser (700–1000 nm, Mira 900, Coherent) or its harmonic generator (360–460 nm). Then, they were directly guided onto the device through an optical fiber. The electrical characterizations were carried out using an Agilent parameter analyzer B1500A.

Supporting Information

Supporting Information is available from the Wiley Online Library or from the author.

Acknowledgements

The authors thank staff in the center of micro-fabrication and characterization of Wuhan national laboratory for optoelectronics for the support in electron-beam lithography and e-beam evaporation. This project was supported by the Natural Science Foundation of China (Grant Nos. 61574066 and 61390504). The authors declare no competing financial interests.

Received: December 22, 2015
Revised: January 26, 2016
Published online:

[1] A. Geim, I. Grigorieva, *Nature* **2013**, *499*, 419.
[2] F. Koppens, T. Mueller, P. Avouris, A. Ferrari, M. Vitiello, M. Polini, *Nat. Nanotechnol.* **2014**, *9*, 780.
[3] M. Buscema, J. O. Island, D. J. Groenendijk, S. I. Blanter, G. A. Steele, H. S. J. V. D. Zant, A. Castellanos-Gomez, *Chem. Soc. Rev.* **2015**, *44*, 3691.
[4] Z. Sun, H. Chang, *ACS Nano* **2014**, *8*, 4133.
[5] F. Bonaccorso, Z. Sun, T. Hasan, A. Ferrari, *Nat. Photonics* **2010**, *4*, 611.
[6] K. S. Novoselov, A. K. Geim, S. Morozov, D. Jiang, Y. Zhang, S. A. Dubonos, I. Grigorieva, A. Firsov, *Science* **2004**, *306*, 666.
[7] K. F. Mak, M. Y. Sfeir, Y. Wu, C. H. Lui, J. A. Misewich, T. F. Heinz, *Phys. Rev. Lett.* **2008**, *101*, 196405.
[8] R. Nair, P. Blake, A. Grigorenko, K. Novoselov, T. Booth, T. Stauber, N. Peres, A. Geim, *Science* **2008**, *320*, 1308.
[9] F. Xia, T. Mueller, Y.-M. Lin, A. Valdes-Garcia, P. Avouris, *Nat. Nanotechnol.* **2009**, *4*, 839.
[10] T. Mueller, F. Xia, P. Avouris, *Nat. Photonics* **2010**, *4*, 297.
[11] F. Schwierz, *Nat. Nanotechnol.* **2010**, *5*, 487.
[12] A. Grigorenko, M. Polini, K. Novoselov, *Nat. Photonics* **2012**, *6*, 749.
[13] F. Xia, H. Yan, P. Avouris, *Proc. IEEE* **2013**, *101*, 1717.
[14] Y.-M. Lin, C. Dimitrakopoulos, K. A. Jenkins, D. B. Farmer, H.-Y. Chiu, A. Grill, P. Avouris, *Science* **2010**, *327*, 662.
[15] Y. Wu, Y.-M. Lin, A. A. Bol, K. A. Jenkins, F. Xia, D. B. Farmer, Y. Zhu, P. Avouris, *Nature* **2011**, *472*, 74.
[16] G. Konstantatos, M. Badioli, L. Gaudreau, J. Osmond, M. Bernechea, F. P. G. de Arquer, F. Gatti, F. H. Koppens, *Nat. Nanotechnol.* **2012**, *7*, 363.
[17] K. F. Mak, C. Lee, J. Hone, J. Shan, T. F. Heinz, *Phys. Rev. Lett.* **2010**, *105*, 136805.
[18] A. Splendiani, L. Sun, Y. Zhang, T. Li, J. Kim, C.-Y. Chim, G. Galli, F. Wang, *Nano Lett.* **2010**, *10*, 1271.
[19] Z. Yin, H. Li, H. Li, L. Jiang, Y. Shi, Y. Sun, G. Lu, Q. Zhang, X. Chen, H. Zhang, *ACS Nano* **2011**, *6*, 74.
[20] W. Choi, M. Y. Cho, A. Konar, J. H. Lee, G. B. Cha, S. C. Hong, S. Kim, J. Kim, D. Jena, J. Joo, *Adv. Mater.* **2012**, *24*, 5832.
[21] O. Lopez-Sanchez, D. Lembke, M. Kayci, A. Radenovic, A. Kis, *Nat. Nanotechnol.* **2013**, *8*, 497.
[22] W. Zhang, J. K. Huang, C. H. Chen, Y. H. Chang, Y. J. Cheng, L. J. Li, *Adv. Mater.* **2013**, *25*, 3456.
[23] D. Warschauer, *J. Appl. Phys.* **1963**, *34*, 1853.
[24] J. Wittig, B. Matthias, *Science* **1968**, *160*, 994.
[25] H. Asahina, A. Morita, *J. Phys. C: Solid State Phys.* **1984**, *17*, 1839.
[26] A. Morita, *Appl. Phys. A* **1986**, *39*, 227.
[27] J. Qiao, X. Kong, Z.-X. Hu, F. Yang, W. Ji, *Nat. Commun.* **2014**, *5*, 4475.
[28] T. Low, A. Rodin, A. Carvalho, Y. Jiang, H. Wang, F. Xia, A. C. Neto, *Phys. Rev. B* **2014**, *90*, 075434.
[29] H. Liu, A. T. Neal, Z. Zhu, Z. Luo, X. Xu, D. Tománek, P. D. Ye, *ACS Nano* **2014**, *8*, 4033.
[30] T. Low, R. Roldán, H. Wang, F. Xia, P. Avouris, L. M. Moreno, F. Guinea, *Phys. Rev. Lett.* **2014**, *113*, 106802.
[31] Y. Du, H. Liu, Y. Deng, P. D. Ye, *ACS Nano* **2014**, *8*, 10035.
[32] L. Li, Y. Yu, G. J. Ye, Q. Ge, X. Ou, H. Wu, D. Feng, X. H. Chen, Y. Zhang, *Nat. Nanotechnol.* **2014**, *9*, 372.
[33] M. Engel, M. Steiner, P. Avouris, *Nano Lett.* **2014**, *14*, 6414.
[34] Y. Deng, N. J. Conrad, Z. Luo, H. Liu, X. Xu, P. D. Ye, presented at *IEEE IEDM,* San Francisco, December 2014, DOI: 10.1109/IEDM.2014.7046987.
[35] Y. Deng, Z. Luo, N. J. Conrad, H. Liu, Y. Gong, S. Najmaei, P. M. Ajayan, J. Lou, X. Xu, P. D. Ye, *ACS Nano* **2014**, *8*, 8292.
[36] N. Youngblood, C. Chen, S. J. Koester, M. Li, *Nat. Photonics* **2015**, *23*, 1.
[37] J. Wu, G. K. W. Koon, D. Xiang, C. Han, C. T. Toh, E. S. Kulkarni, I. Verzhbitskiy, A. Carvalho, A. S. Rodin, S. P. Koenig, *ACS Nano* **2015**, *9*, 8070.
[38] F. Xia, H. Wang, Y. Jia, *Nat. Commun.* **2014**, *5*, 4458.
[39] T. Hong, B. Chamlagain, W. Lin, H.-J. Chuang, M. Pan, Z. Zhou, Y.-Q. Xu, *Nanoscale* **2014**, *6*, 8978.
[40] H. Yuan, X. Liu, F. Afshinmanesh, W. Li, G. Xu, J. Sun, B. Lian, A. G. Curto, G. Ye, Y. Hikita, *Nat. Nanotechnol.* **2015**, *10*, 707.
[41] Y. Chen, G. Jiang, S. Chen, Z. Guo, X. Yu, C. Zhao, H. Zhang, Q. Bao, S. Wen, D. Tang, D. Fan, *Opt. Express* **2015**, *23*, 12823.
[42] S. B. Lu, L. L. Miao, Z. N. Guo, X. Qi, C. J. Zhao, H. Zhang, S. C. Wen, D. Y. Tang, D. Y. Fan, *Opt. Express* **2015**, *23*, 11183.
[43] Z. Guo, H. Zhang, S. Lu, Z. Wang, S. Tang, J. Shao, Z. Sun, H. Xie, H. Wang, X. Yu, P. K. Chu, *Adv. Funct. Mater.* **2015**, *25*, 6696.
[44] S. Das, H.-Y. Chen, A. V. Penumatcha, J. Appenzeller, *Nano Lett.* **2012**, *13*, 100.
[45] X. Li, L. Yang, M. Si, S. Li, M. Huang, P. Ye, Y. Wu, *Adv. Mater.* **2015**, *27*, 1547.
[46] M. Buscema, D. J. Groenendijk, S. I. Blanter, G. A. Steele, H. S. van der Zant, A. Castellanos-Gomez, *Nano Lett.* **2014**, *14*, 3347.
[47] M. Buscema, D. J. Groenendijk, G. A. Steele, H. S. van der Zant, A. Castellanos-Gomez, *Nat. Commun.* **2014**, *5*, 4651.
[48] B. Liu, M. Köpf, A. N. Abbas, X. Wang, Q. Guo, Y. Jia, F. Xia, R. Weihrich, F. Bachhuber, F. Pielnhofer, H. Wang, R. Dhall, S. B. Cronin, M. Ge, X. Fang, T. Nilges, C. Zhou, *Adv. Mater.* **2015**, *27*, 4423.
[49] L. Dou, Y. M. Yang, J. You, Z. Hong, W.-H. Chang, G. Li, Y. Yang, *Nat. Commun.* **2014**, *5*, 5404.